Interdiffusion-controlled Kondo suppression of injection efficiency in metallic nonlocal spin valves

L. O'Brien,[1,2] D. Spivak,[3] J. S. Jeong,[1] K. A. Mkhoyan,[1] P. A. Crowell,[3] and C. Leighton[1,*]

[1]*Department of Chemical Engineering and Materials Science, University of Minnesota, Minnesota, 55455 USA*
[2]*Thin Film Magnetism, Cavendish Laboratory, University of Cambridge, CB3 0HE UK*
[3]*School of Physics and Astronomy, University of Minnesota, Minnesota, 55455 USA*

Nonlocal spin valves (NLSVs) generate pure spin currents, providing unique insight into spin injection and relaxation at the nanoscale. Recently it was shown that the puzzling low temperature nonmonotonicity of the spin accumulation in all-metal NLSVs occurs due to a manifestation of the Kondo effect arising from dilute local-moment-forming impurities in the nonmagnetic material. Here it is demonstrated that precise control over interdiffusion in Fe/Cu NLSVs via thermal annealing can induce dramatic increases in this Kondo suppression of injection efficiency, observation of injector/detector separation-dependent Kondo effects in both charge and spin channels simultaneously, and, in the limit of large interdiffusion, complete breakdown of standard Valet-Fert-based models. The Kondo effect in the charge channel enables extraction of the exact interdiffusion profile, quantifying the influence of local moment density on the injection efficiency and presenting a well-posed challenge to theory.

Improved understanding of spin transport in metals is important for the development of low resistance alternatives to the tunnel magnetoresistance [1–4] field sensors used in hard disk drive read heads and will require a substantial increase in the current knowledge of spin injection and relaxation in metals [5]. Because they enable separation of charge and spin currents, nonlocal spin valves (NLSVs) [6] provide critical insight into these issues, particularly at the nanoscale [7]. In the nonlocal geometry [inset, Fig. 1(b)] two ferromagnetic metal (FM) electrodes are separated by a distance d and are connected by a nonmagnetic metal (NM) channel. Controlled by the current polarization in the FM, $\alpha_{FM} = (I_\uparrow - I_\downarrow)/(I_\uparrow + I_\downarrow)$, a charge current driven from the FM injector into the NM generates a nonequilibrium spin accumulation in the NM and a pure spin current between the two FMs. The spin imbalance decays on a length scale λ_N, the NM spin diffusion length, and some fraction of the spin accumulation thus persists at the FM detector. This results in a chemical potential difference V_{NL} between the FM detector and the NM far from the FM, which is modulated by toggling the magnetizations of the FMs between parallel and antiparallel. The resulting nonlocal spin resistance, $\Delta R_{NL} = \Delta V_{NL}/I$, provides a direct probe of the spin accumulation and, thus, λ_N [via $\Delta R_{NL}(d)$].

Contrary to simple expectations based on Elliott-Yafet spin relaxation [8–10], $\Delta R_{NL}(T)$ is observed to be nonmonotonic in many all-metal NLSVs, first increasing on cooling, but then decreasing at low T [11–17]. This T dependence has recently been explained as a manifestation of the Kondo effect [18,19], due to dilute local-moment-forming FM impurities in the NM [20]. In essence, the interaction of the NM conduction electrons with impurity virtual bound states as they screen the randomly oriented FM impurity moments induces depolarization of the injected spin current around the Kondo temperature T_K. This occurs even in NM channels prepared from impurity-free source materials, due to inevitable chemical interdiffusion between the FMs and the NM at interfaces

[20]. NM contamination due to finite source purity, or transfer of FM impurities from resists, has also been discussed [12,13], with a recent paper [21] confirming previous statements [20] that the Kondo effect will impact λ_N in addition to suppressing current polarization in channels uniformly contaminated with FM impurities. As expected, in the interdiffused case the nonmonotonic behavior of $\Delta R_{NL}(T)$ is observed only for combinations of FM and NM in which isolated impurities of the FM form local moments in the NM, and hence no peak is observed when Al is used as a NM [20]. Despite such progress, much remains to be understood about this effect, including the detailed mechanism causing depolarization of the spin current and the dependence on interdiffusion, impurity concentration, etc.

In this paper, fine control over the interdiffusion profile between FM contacts and a NM channel via thermal annealing of Fe/Cu NLSVs is demonstrated, enabling direct study of the relationship between the Fe impurity concentration $C_{Fe}(x)$ in the Cu and the low T Kondo suppression of spin accumulation. Increasing the annealing temperature (T_A), and thus the extent of interdiffusion, is found to lead to a strong increase in Kondo-induced depolarization and eventually to breakdown of one-dimensional (1D) solutions based on the Valet-Fert (V-F) formalism [22,23]. Moreover, promoting interdiffusion out to mesoscopic length scales is shown to lead to d-dependent Kondo effects in both charge and spin channels. The d dependence of the charge Kondo effect then enables precise determination of $C_{Fe}(x)$, validated against scanning transmission electron microscopy/energy dispersive x-ray spectroscopy (STEM/EDX) characterization. The relation between the Fe diffusion length ℓ_{Fe} and the Kondo suppression of injection efficiency is thus obtained, providing a well-defined result with which to test future theory in this technologically and fundamentally important class of canonical spin transport devices.

The devices studied here were fabricated on Si/SiN substrates by electron-beam lithography. Multiangle Fe and Cu electron beam evaporation (base pressure $< 10^{-9}$ Torr) through a suspended resist mask was employed to avoid intermediate air exposure [24,25]. Growth rates and pressures
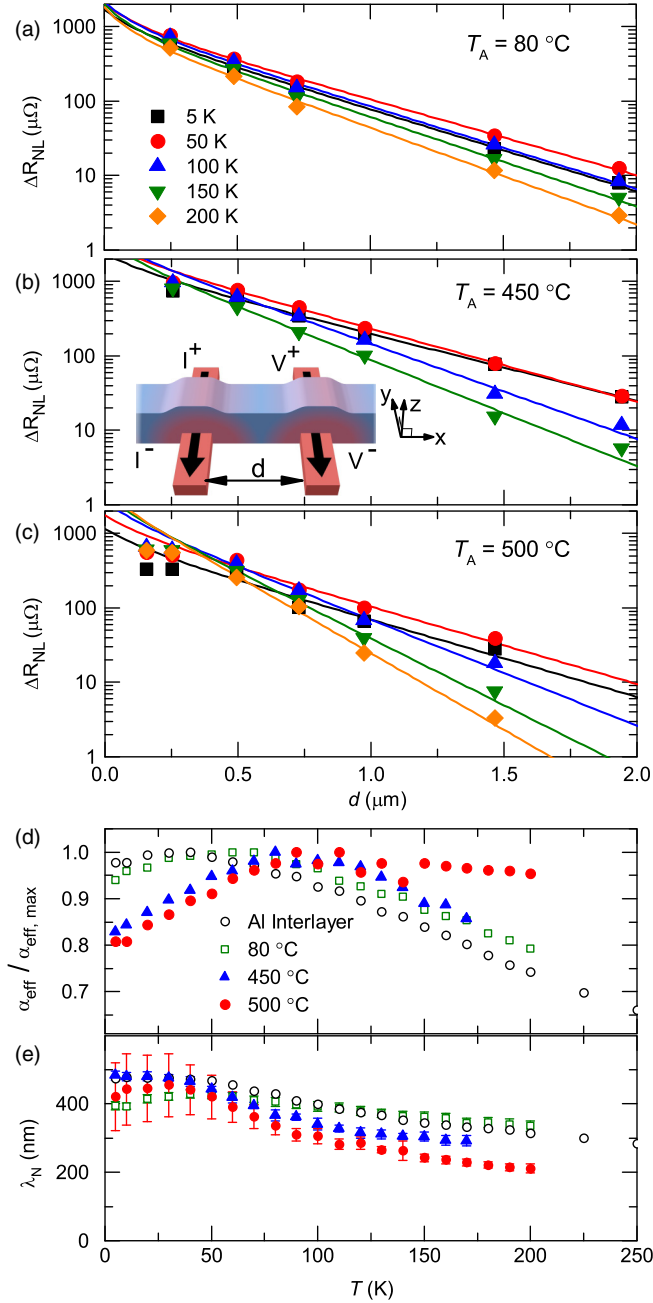
---

*Corresponding author: leighton@umn.edu

FIG. 1. *d* dependence of ΔR_{NL} at 5, 50, 100, 150, and 200 K for devices annealed at $T_A = 80\,°\mathrm{C}$ (a), 450 °C (b), and 500 °C (c). Solid lines are fits to Eq. (1). The inset to (b) is a schematic, depicting an NLSV with FM/NM interdiffusion. *T* dependence of (d) α_{eff}, normalized to its maximum, as extracted from fits to $\Delta R_{\mathrm{NL}}(d,T)$, and (e) the corresponding λ_N. Data are shown for devices with a 5 nm Al interlayer, and devices annealed at $T_A = 80$, 450, and 500 °C.

were: 0.5 Å/s, 1×10^{-9} Torr; and 1 Å/s, 1×10^{-8} Torr, for Fe and Cu, respectively, and the nominal Cu source purity was 99.999% (i.e., $C_{\mathrm{Fe}} < 10$ parts per million [ppm]). Fe/Cu is chosen as illustrative because dilute quantities of Fe are both miscible and moment-forming in Cu [26,27], with $T_K = 30$ K. FM injector, FM detector, and NM channel widths and thicknesses were $w_{\mathrm{FM,inj}} = 150$ nm, $w_{\mathrm{FM,det}} = 100$ nm, $w_N = 150$ nm; and $t_{\mathrm{FM}} = 16$ nm, $t_N = 200$ nm. The FM

injector/detector separation *d* was varied between 150 nm and 5 μm. Postfabrication annealing was performed under high vacuum (10^{-6} Torr) at various T_A for 2 h. For structural/chemical characterization, STEM specimens were prepared using a 30 kV focused ion beam (FEI Quanta 200 3D) followed by 5 kV Ga ion milling, enabling cross-sectional imaging of NLSVs in the *x-z* plane [see inset, Fig. 1(b)]. An aberration-corrected FEI Titan G2 60–300 STEM equipped with a Super-X EDX system was used, operating at 300 kV. The measured transmission electron microscopy (TEM) specimen thicknesses, using low-loss electron energy loss spectroscopy, were approximately 72 and 94 nm, respectively, for $T_A = 80$ and 450 °C. Considering the effects of convergent beam broadening, channelling, and beam-specimen interaction gives an estimate of intrinsic interface broadening of <1 nm, significantly smaller than the observed interface widths in this paper. Methods for transport measurements were reported in more detail in Ref. [20]. They involve ac excitation at 13 Hz with bias currents of 100 μA. ΔR_{NL} was independent of excitation current in the regime investigated.

Figures 1(a)–1(c) show $\Delta R_{\mathrm{NL}}(d)$ at various *T*, for both unannealed devices [Fig. 1(a)], and devices annealed at $T_A = 450$ [Fig. 1(b)] and 500 °C [Fig. 1(c)]. (In the unannealed case, the T_A quoted [80°C] is the highest *T* experienced during processing.) Other T_A values were measured and will be summarized later, but the focus for now is placed on the illustrative values 80, 450, and 500 °C. The ΔR_{NL} in unannealed devices [Fig. 1(a)] decreases with increasing *d*, as expected, with the nonmonotonic *T* dependence discussed above. Specifically, at a given *d*, ΔR_{NL} first increases on cooling, before decreasing below 50 K due to the Kondo mechanism [20]. As T_A increases, the low *T* suppression of ΔR_{NL} becomes much more apparent, particularly at small *d* [e.g. Fig. 1(c)]. This suggests increased Kondo suppression of ΔR_{NL} when interdiffusion is promoted by annealing. To quantify this observation, $\Delta R_{\mathrm{NL}}(d)$ was fit to a standard 1D solution to the V-F model [23] for NLSVs in the transparent interface limit [22]. This is the limit $R_I, R_{\mathrm{FM}} < R_N$, where R_I is the FM/NM contact resistance, and R_{FM}, R_N are the spin resistances, $R_{\mathrm{FM}} = \rho_{\mathrm{FM}} \lambda_{\mathrm{FM}} / w_N w_{\mathrm{FM}}$ and $R_N = \rho_N \lambda_N / w_N t_N$. Here, λ_{FM} is the spin diffusion length in the FM, and ρ_N and ρ_{FM} are the NM/FM resistivities. Operation in the transparent limit was verified by the magnitude (and sign) of R_I from three-terminal measurements, the nonexponential dependence of ΔR_{NL} on *d* (see below), and the existence of FM-induced dephasing in four-terminal Hanle measurements (see supplementary discussion in Ref. [20] for more details). In this limit [22]:

$$\Delta R_{\mathrm{NL}}(d,T) = 4 \frac{\alpha_{\mathrm{eff}}^2 R_{\mathrm{FM}}^2}{(1 - \alpha_{\mathrm{eff}}^2)^2 R_N}$$
$$\times \frac{\exp(-d/\lambda_N)}{\left[1 + \frac{2R_{\mathrm{FM}}}{(1 - \alpha_{\mathrm{eff}}^2) R_N}\right]^2 - \exp(-2d/\lambda_N)}, \quad (1)$$

where we define α_{eff} as an *effective* value of α_{FM}. This is done because, at least with the fabrication methods used here, the Kondo suppression of $\Delta R_{\mathrm{NL}}(T)$ is determined by local moments formed by interdiffusion at the FM/NM interfaces. In Eq. (1) this near-interface effect is manifest as a low *T*

suppression of α_{FM}, rather than $\lambda_N(T)$. This distinguishes α_{eff} from α_{FM}, an intrinsic property of the FM. Additionally, at high T_A, interfacial alloying is anticipated, rendering the extracted polarization a property more of the interfacial Fe-Cu alloy than pure Fe. For these reasons we also emphasize below the T dependence of α_{eff}, rather than its absolute values; the latter are nevertheless discussed in Appendix. It is essential to fix as many parameters in Eq. (1) as possible. Therefore, $\rho_N(T)$ is measured on each NLSV, $\rho_{\mathrm{FM}}(T)$ is measured on FM nanowires with identical dimensions and growth/annealing parameters, and all physical dimensions in Eq. (1) are determined by microscopy. This leaves λ_N, λ_{FM}, and α_{eff} as free parameters. As described earlier [20], determining λ_{FM} from ρ_{FM} via an empirical relationship [5] is an effective parameter constraint, resulting in $\lambda_{\mathrm{Fe}} \approx 4\,\mathrm{nm}$. This leaves only λ_N and α_{eff} as fitting parameters. Moreover, Eq. (1) reduces to a single exponential when $d > \lambda_N$, directly yielding λ_N. λ_N and α_{eff} are thus easily separable.

The solid lines in Figs. 1(a)–1(c) are fits to Eq. (1) with the discussed approach. For $T_A = 80\,^\circ\mathrm{C}$ [Fig. 1(a)], good fits are obtained, highlighting the simple exponential behavior at large d and the upward deviation at low d, which is a defining characteristic of transparent interfaces. At $T_A = 450$ and $500\,^\circ\mathrm{C}$ [Figs. 1(b) and 1(c)], the high-d single exponential fall-off is maintained, but with increasingly large departures at low d and T due to the Kondo suppression of injection efficiency. The magnitude of these departures at low d is surprising, constituting breakdown of the standard V-F model at only modest (see below) levels of FM/NM interdiffusion, highlighting the remarkable efficiency with which dilute FM impurities relax spin. This Kondo suppression is illustrated in Figs. 1(d) and 1(e), in which the extracted $\alpha_{\mathrm{eff}}(T)$ (normalized to its maximum, α_{max}; absolute values of α_{eff} are shown in Appendix) and $\lambda_N(T)$ are shown vs. T_A. Note that for $T_A = 450$ and $500\,^\circ\mathrm{C}$, the values shown are from fits of $\Delta R_{\mathrm{NL}}(d)$ in the region $d \geqslant 500\,\mathrm{nm}$ [Figs. 1(b) and 1(c)], which must be borne in mind when considering extracted α_{eff} values. In this, and all subsequent plots, we use green, blue, and red for $T_A = 80, 450$, and $500\,^\circ\mathrm{C}$, respectively. Also shown in Figs. 1(d) and 1(e) are data from an NLSV with a thin ($\sim 5\,\mathrm{nm}$) Al interlayer (IL) between the Fe and Cu. As described in Ref. [20], the Al both inhibits interdiffusion and quenches local moments (Al does not support local moments on Fe impurities), eliminating the Kondo suppression of α_{FM}. The Al IL data thus show nearly monotonic increases in α_{eff} and λ_N on cooling. Moving to the non-IL devices, at $T_A = 80\,^\circ\mathrm{C}$ a low T downturn in α_{eff} becomes more noticeable, reaching $\sim 6\%$. At $T_A = 450$ and $500\,^\circ\mathrm{C}$, however, the low T suppression is significantly increased, α_{eff} decreasing by $\sim 20\%$ between 100 and 5 K. Annealing therefore promotes Fe/Cu interdiffusion, increasing C_{Fe} near the interface, and thus both the magnitude and onset T of the α_{eff} suppression. This occurs in the absence of strong effects in $\lambda_N(T)$, which saturates at low T at 400–500 nm. It should be emphasized, again, that Kondo effects being more visible in $\alpha_{\mathrm{eff}}(T)$ than $\lambda_N(T)$ is due to the fact that in this case the magnetic impurities are more concentrated in the near-interface regions, rather than the bulk of the channel. As the magnetic impurity density in the bulk of the channel increases, Kondo effects should become visible also in $\lambda_N(T)$ [21]. There may be some evidence of

this at $T_A = 500\,^\circ\mathrm{C}$ in Fig. 1(e), although the error bars are significant in that case due to the increased fitting error when $\Delta R_{\mathrm{NL}}(d)$ departs from the form of Eq. (1) [Fig. 1(c)].

A more detailed view of the dependence of $\Delta R_{\mathrm{NL}}(T)$ on d and T_A is provided in Fig. 2 (upper panels), where the suppression of ΔR_{NL} below some temperature T_{max} is clear. Also shown in Fig. 2 (lower panels) are the corresponding $\rho_N(T)$ data, plotted as $\rho_N(T)/\rho_{\mathrm{min}}$, where ρ_{min} is the minimum value of ρ_N. Starting at $T_A = 80\,^\circ\mathrm{C}$ [Fig. 2(a)], the low T suppression in ΔR_{NL} is clearly observable, with both the magnitude ($\sim 13\%$ reduction at $d = 250\,\mathrm{nm}$) and T_{max} ($\sim 70\,\mathrm{K}$) comparing well to prior papers [11–13,15,17,28]. The corresponding $\rho_N(T)/\rho_{\mathrm{min}}$ [Fig. 2(d)] reveals barely any indication of the Kondo effect in charge transport (a weak minimum is actually present at $\sim 12\,\mathrm{K}$), due to the majority of the current flowing through the low resistivity "bulk" of the NM, in which C_{Fe} is negligible [20]. Moving straight to the highest annealing temperature, $T_A = 500\,^\circ\mathrm{C}$, Figs. 2(c) and 2(f) reveal very different behavior. The Kondo suppression of ΔR_{NL} is dramatically enhanced, $\Delta R_{\mathrm{NL}}(d = 250\,\mathrm{nm})$ decreasing by $\sim 50\%$ below $T_{\mathrm{max}} \approx 120\,\mathrm{K}$. Additionally, a clear signature of the Kondo effect emerges in the charge channel, with a minimum developing in $\rho_N(T)$ at $T_{\mathrm{min}} = 18.5\,\mathrm{K}$. It is important to note here that although both effects are Kondo derived, the T_{max} in $\Delta R_{\mathrm{NL}}(T)$ and the T_{min} in $\rho_N(T)$ do not coincide with each other or with T_K (30 K). This is because T_{max} is determined by $\alpha_{\mathrm{eff}}(T)$, $\rho_{N,\mathrm{FM}}(T)$, and $\lambda_{N,\mathrm{FM}}(T)$, whereas T_{min} is controlled by the relative contributions of phonon and Kondo scattering to $\rho_N(T)$. Nonetheless, it is clear from Figs. 2(c) and 2(f) that $500\,^\circ\mathrm{C}$ annealing promotes interdiffusion to such a degree that nonnegligible values of C_{Fe} occur throughout the NM [note the d independence in Fig. 2(f)], inducing large Kondo effects in both spin [ΔR_{NL}, Fig. 2(c)] and charge transport [ρ_N, Fig. 2(f)]. The most interesting result, however, is obtained at the intermediate annealing temperature, $T_A = 450\,^\circ\mathrm{C}$ [Figs. 2(b) and 2(e)]. Here, the maximum in ΔR_{NL} and minimum in $\rho_N(T)$ are of course intermediate between $T_A = 80$ and $500\,^\circ\mathrm{C}$, but $\rho_N(T)/\rho_{\mathrm{min}}$ is also now *strongly d dependent* [Fig. 2(e)]. Both T_{min} and the strength of the Kondo minimum increase as d decreases, indicating that at $T_A = 450\,^\circ\mathrm{C}$, a clear gradient in $C_{\mathrm{Fe}}(x)$ occurs along the NM channel, resulting in a d-dependent strength of the Kondo effect. This concentration gradient is illustrated by the color gradient in the inset to Fig. 1(b). Note that from Fig. 2 it appears that increasing annealing temperature from 80 to $450\,^\circ\mathrm{C}$ increases $\Delta R_{\mathrm{NL}}(d,T)$. Care must be taken, however, as variations in FM and NM dimensions (between samples), or ρ_N, R_I, λ_{FM}, or α_{FM} (with annealing) can cause systematic differences in $\Delta R_{\mathrm{NL}}(d,T)$.

Importantly, the $\rho_N(T)$ data shown in Figs. 2(d)–2(f) enable, in conjunction with established knowledge of the conventional Kondo effect for Fe in Cu, extraction of the average value $\langle C_{\mathrm{Fe}} \rangle$ of C_{Fe} in the NM as a function of d and T_A. To do this, $\rho_N(T)$ around T_{min} is fit to the simple form [29]:

$$\rho_N(T) = \rho_0 + AT^5 - \rho_K \log T/T_K, \qquad (2)$$

where ρ_0 accounts for T-independent impurity scattering, the AT^5 term for phonon scattering, and the ρ_K term for the charge Kondo effect. Because $\rho_K \propto \langle C_{\mathrm{Fe}} \rangle$, in this simple case then
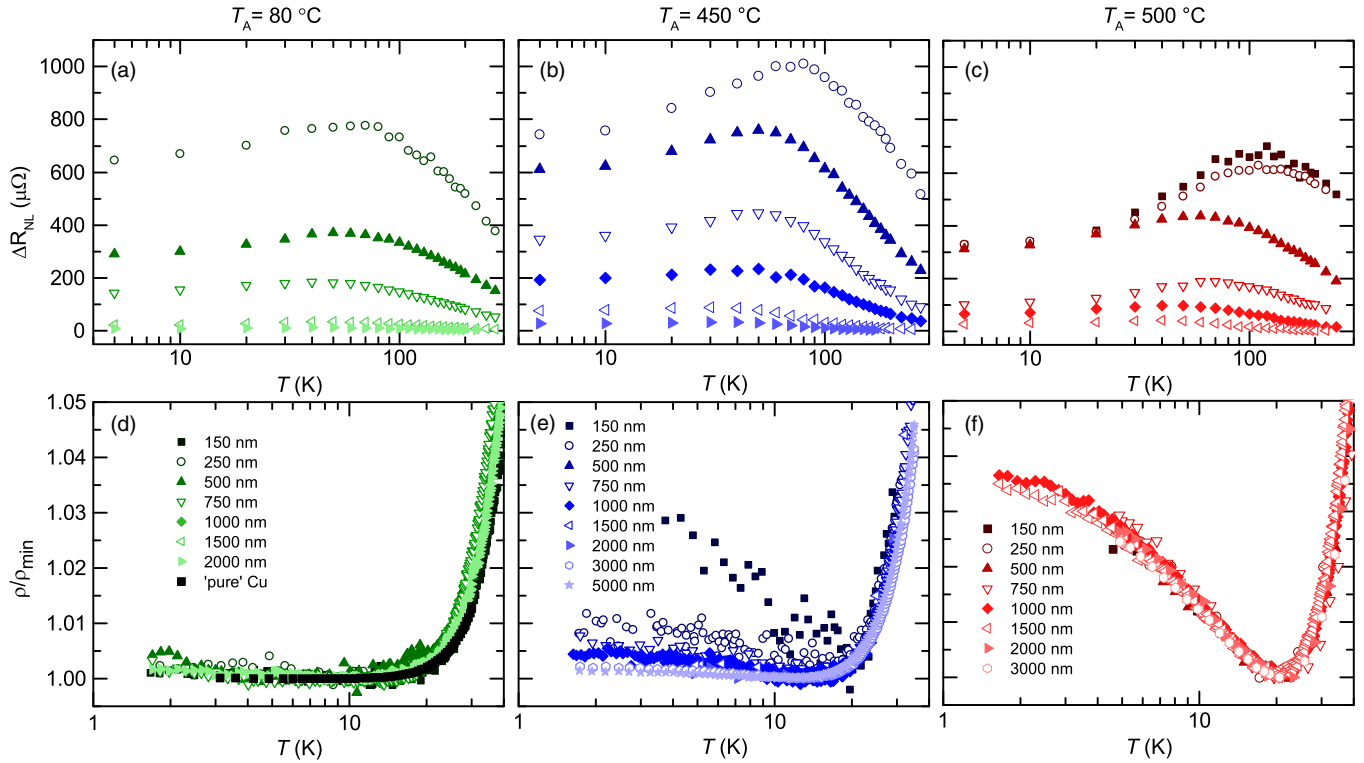
FIG. 2. $\Delta R_{\mathrm{NL}}(T)$, for various d, for $T_A = 80\,^\circ\mathrm{C}$ (a), $450\,^\circ\mathrm{C}$ (b) and $500\,^\circ\mathrm{C}$ (c). (d,e,f) Corresponding low temperature $\rho_N(T)/\rho_{\mathrm{min}}$. Note the logarithmic T axes, with different scales for $\Delta R_{\mathrm{NL}}(T)$ and $\rho_N(T)$.

$T_{\mathrm{min}} = \eta \langle C_{\mathrm{Fe}} \rangle^{1/5}$ [30], where η is a constant known from prior work [31] (8.07 K with $\langle C_{\mathrm{Fe}} \rangle$ in parts per million). Fitting the data of Figs. 2(d)–2(f) with Eq. (2) yields the $T_{\mathrm{min}}(d)$ data shown in Fig. 3(a). Note the relatively high, d-independent T_{min} at $T_A = 500\,^\circ\mathrm{C}$ and the strongly d-dependent T_{min} at $T_A = 450\,^\circ\mathrm{C}$. These $T_{\mathrm{min}}(d)$ data can then be converted to $\langle C_{\mathrm{Fe}}(d) \rangle$ [Fig. 3(b)], from which it is clear that the T_A range investigated encompasses three regimes. At low $T_A (80\,^\circ\mathrm{C})$, interdiffusion is limited to the near interface region. Only a trace concentration of Fe is detected in the bulk of the NM ($\sim$7 ppm), in line with the nominal Cu source purity. At intermediate $T_A (450\,^\circ\mathrm{C})$, substantial interdiffusion occurs, over mesoscopic scales, resulting in a d-dependent $\langle C_{\mathrm{Fe}} \rangle$. In essence, the diffusion length for Fe into Cu at $T_A = 450\,^\circ\mathrm{C}$ becomes comparable to the d range probed (hundreds of nanometers). Finally, at high T_A ($500\,^\circ\mathrm{C}$), the diffusion length significantly exceeds the probed d range, and $\langle C_{\mathrm{Fe}} \rangle$ assumes a relatively large d-independent value (at least at the d values probed here) of $\sim$63 ppm.

Qualitatively, this interdiffusion behavior is consistent with expectations for thermally activated interdiffusion in polycrystalline metals, where diffusion occurs both via grain (G) and grain boundary (GB) mechanisms [32,33]. These have characteristic activation energies (Q_G, Q_{GB}) and diffusion lengths [$\ell_{\mathrm{Fe}}^G(T_A), \ell_{\mathrm{Fe}}^{\mathrm{GB}}(T_A)$]. Figure 3(c) shows a "phase map" for G (ℓ_{Fe}^G, blue curve) and GB diffusion ($\ell_{\mathrm{Fe}}^{\mathrm{GB}}$, orange curves), assuming a thermally activated process of the form $\ell_{\mathrm{Fe}} = \sqrt{Dt}$, with Fe diffusivity $D = D_0 \exp(-Q/k_B T_A)$, and activation energy Q. We take the annealing time $t = 2$ h; $D_0 = 1 \times 10^{-5}$ m^2/s for both G and GB diffusion [34]; $Q_G = 2.21$ eV [35,36]; and $Q_{\mathrm{GB}} = \beta Q_G$, with the region between the

orange lines indicating $\ell_{\mathrm{Fe}}^{\mathrm{GB}}$ for $0.4 < \beta < 0.6$, as is typical in polycrystalline face-centered cubic and body-centered cubic metals [34]. To indicate the relevant length scales in this paper, also shown as horizontal lines in Fig. 3(c) are the average in-plane grain size, g_{avg} (measured via TEM), and characteristic channel length, d_{char}. Considering this figure, the physical origins of the three experimentally observed interdiffusion regimes become clear [as shown schematically in Figs. 3(d)–3(f)]. At low T_A ($<300\,^\circ\mathrm{C}$), interdiffusion via both G and GB is frozen out, and C_{Fe} throughout the NM channel is low [Fig. 3(d)]. At intermediate T_A ($\sim$450 $^\circ\mathrm{C}$), $\ell_{\mathrm{Fe}}^{\mathrm{GB}} \sim d_{\mathrm{char}}$ but $\ell_{\mathrm{Fe}}^G < g_{\mathrm{avg}}$; C_{Fe} thus becomes separation-dependent on the length scales relevant to our devices, with diffusion preferentially via GBs [Fig. 3(e)]. Finally, at high T_A ($\geqslant 500\,^\circ\mathrm{C}$) the GBs essentially "short circuit" the Fe diffusion, the channel becoming uniformly "doped" with a high C_{Fe}, while diffusion from the GB into the G commences [Fig. 3(f)]. At this point, the Cu channel "doping" is d independent [as seen in Fig. 3(b)]. It is noted that (a) the Kondo effect in charge transport is one of the few ways one could imagine quantifying the parts-per-million-level chemical profile in these devices and (b) the comparison of $\Delta R_{\mathrm{NL}}(d,T)$ and $\rho_N(d,T)$ in Fig. 2, and the above analysis, clearly illustrate which parameters set T_{max} and T_{min}, expanding our understanding over Ref. [20].

To quantify the above statements regarding diffusion mechanisms, and directly probe ℓ_{Fe} in these devices, STEM/EDX was performed. Figures 4(a) and 4(b) show representative cross-sectional EDX maps of Fe, Cu, and Si [in the x-z plane, as indicated in the inset to Fig. 1(b)] of Fe/Cu NLSVs annealed at 80 and 450 $^\circ\mathrm{C}$. Not only are the Fe injector/detector, Cu channel, and Si substrate clearly observed, but it is also
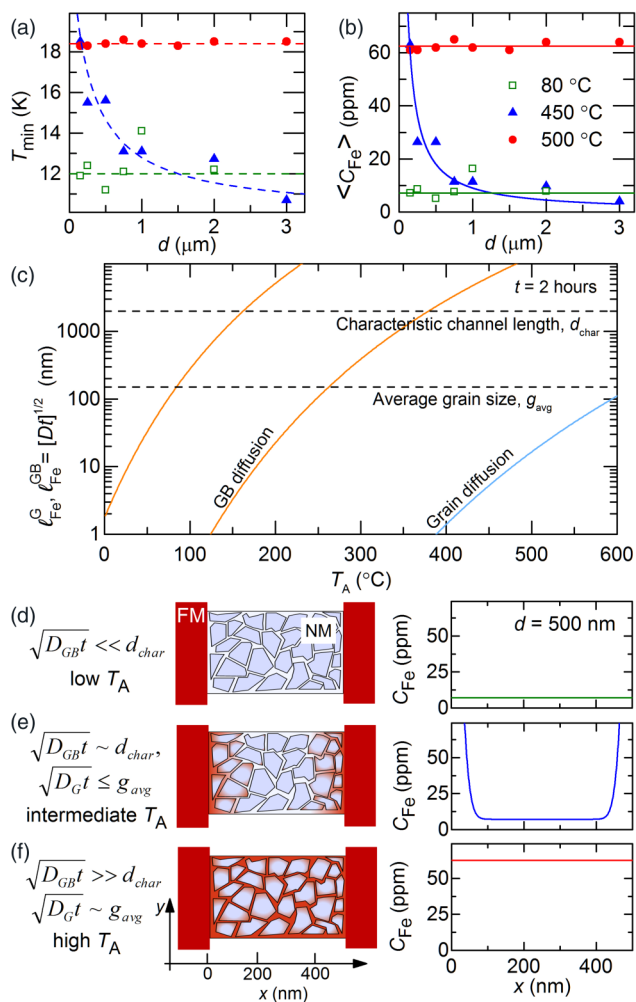
FIG. 3. (a) d dependence of $T_{\min}$ for $T_A = 80$, 450, and 500 °C. Dashed lines are guides to the eye. (b) d dependence of $\langle C_{Fe} \rangle$ from $T_{\min} = \eta \langle C_{Fe} \rangle^{1/5}$, with $\eta = 8.07$ K. Solid lines are fits based on constant concentration (80 and 500 °C) or a semi-infinite-medium interdiffusion model (450 °C anneal, ℓ_{Fe} 12.4 nm). (c) Fe diffusion length in Cu, ℓ_{Fe}, as a function of annealing temperature T_A, for two interdiffusion mechanisms: "bulk" grain diffusion (ℓ_{Fe}^G) and grain boundary (GB) diffusion (ℓ_{Fe}^{GB}). The orange curves represent the region for GB diffusion using the range of activation energies given in the text. Also shown are the average in-plane grain size, g_{avg}, and characteristic channel length, d_{char}. All data are for an anneal time of $t = 2$ h. (d,e,f) Schematics of three possible diffusion profiles in polycrystals.

seen that the Fe/Cu interface is significantly interdiffused for $T_A = 450$ °C [Fig. 4(b)]. Due to asymmetry in the in-plane vs. out-of-plane grain dimensions, and so the weighting of G to GB diffusion, ℓ_{Fe} is somewhat anisotropic [Figs. 4(a) and 4(b)]. Despite this asymmetry, in-plane and out-of-plane ℓ_{Fe} values scale similarly with T_A. Moreover, the interdiffusion of Fe through the Cu channel will be determined by the in-plane ℓ_{Fe}, due to the relative scale of the channel length (micrometers) and width (200 nm) compared with the channel height (200 nm). As such, only the in-plane value of ℓ_{Fe} is discussed here. Figures 4(c) and 4(d) show line scans of the in-plane $C_{Fe}(x)$ through the FM, surrounded by NM. The solid lines
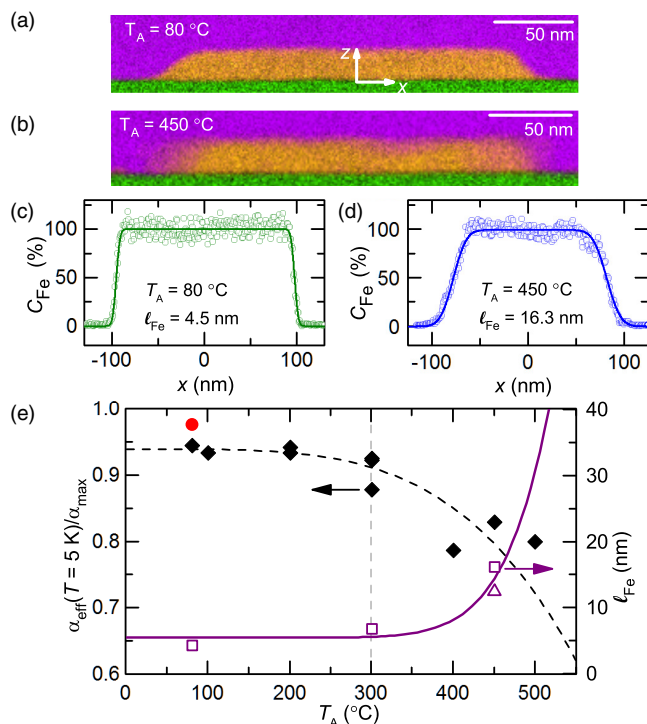

FIG. 4. (a,b) STEM/EDX maps (purple, Cu; orange, Fe; green, Si) at $T_A = 80$ and 450 °C. (c,d) Lateral EDX line scans of $C_{Fe}(x)$ (open circles); the solid lines are fits to a semi-infinite-medium diffusion model. (e) $\alpha_{eff}(T = 5$ K), normalized to α_{max}, as a function of T_A (black diamonds, left axis). The red circle indicates an Fe/Al IL/Cu device. The open purple data (right axis) show $\ell_{Fe}(T_A)$ from Kondo (triangle) and STEM/EDX (squares) analyses. The solid purple line is a fit to a two-channel interdiffusion model.

in Figs. 4(c) and 4(d) are fits to a 1D semi-infinite diffusion profile at each interface, $C_{Fe} \propto 1 - \text{erf}(x/\ell_{Fe})$, resulting in $\ell_{Fe} = 4.5$ nm at $T_A = 80$ °C, increasing fourfold to 16.3 nm at $T_A = 450$ °C. Such measurements of course only probe C_{Fe} in the interface region, being insensitive to the sub-100 ppm tails of the interdiffusion profile relevant to Kondo physics.

To determine ℓ_{Fe} further from the FM/NM interfaces, $\langle C_{Fe} \rangle$ from Fig. 3(b) was also fit with a 1D semi-infinite slab diffusion approach. In doing this, it is important to recognize, of course, that the charge Kondo effect arises from dilute local moments dissolved in the NM host. Above the bulk solubility limit of Fe in Cu, at least in the thermodynamic limit, Fe will precipitate out of the Cu host and form phase-segregated clusters, which we anticipate make little Kondo contribution to $\rho_N(T)$. We therefore expect that any measure of $\langle C_{Fe} \rangle$ from the Kondo effect will be sensitive only to the average $C_{Fe}(x)$ in the main phase solid $Cu_{1-x}Fe_x$ solution. To account for this, we assume $C_{Fe}(x)$ in Fig. 3(b) is sensitive only to the intercontact region of the channel, where C_{Fe} is below the bulk solubility limit [37] (∼2600 ppm) [i.e., beyond some distance d_0 from each FM/NM interface (with $C_{Fe}(d_0) = 2600$ ppm)]. The results in Fig. 4(d) give $d_0 = 32$ nm for $T_A = 450$ °C. To determine ℓ_{Fe} at $T_A = 450$ °C from the charge Kondo effect, $\langle C_{Fe}(d) \rangle$ [see Fig. 3(b)] was fit to a semi-infinite 1D diffusion profile over this dilute region, accounting for diffusion from

each contact:

$$C_{Fe}(x,d) = \left(1 - \mathrm{erf}\left(\frac{x}{\ell_{Fe}}\right)\right) + \left(1 + \mathrm{erf}\left(\frac{d-x}{\ell_{Fe}}\right)\right), \quad (3)$$

$$\langle C_{Fe}(d)\rangle = \frac{1}{d-2d_0}\int_{d_0}^{d-d_0} C_{Fe}\, dx. \quad (4)$$

The solid blue line in Fig. 3(b) shows the result of such fitting. The data are well described with $\ell_{Fe}(T_A = 450\,°C) = 12.4$ nm, in very reasonable agreement with the 16.3 nm obtained from EDX. The near interface EDX concentration [Fig. 4(d)] is thus consistent with the parts-per-million-level tail from analysis of the charge Kondo effect [Fig. 3(b)].

The right axis of Fig. 4(e) shows $\ell_{Fe}(T_A)$ determined via these two methods [i.e., EDX (open squares) and the charge Kondo effect (open triangle)]. Significantly, the solid line through the data is a fit to a two-channel 1D model (G and GB diffusion), quantitatively accounting for both mechanisms by using an effective $\ell_{Fe} = m\ell_{Fe}^{GB} + (1-m)\ell_{Fe}^{G} + \ell_0$. Here, $m = \delta/g_{avg}$ is a weighting factor to account for the relative cross-sectional areal density of G to GBs; δ is the GB width, and ℓ_0 accounts for any interdiffusion that occurs outside the annealing process [32,33]. Here, we take $\delta = 0.5$ nm, $g_{avg} = 150$ nm (as established from STEM analysis), $Q_G = 2.21$ eV [35,36], and $D_0 = 1 \times 10^{-5}$ m^2/s [34], leaving only β and ℓ_0 as free parameters. The fit describes the data well, with $Q_{GB}/Q_B = 0.7$ and an ℓ_0 (the unannealed Fe interdiffusion length) of 5.3 nm. Both values are entirely reasonable, Q_{GB}/Q_B being consistent with literature values [33], while ℓ_0 lies close to the unannealed EDX result (4.5 nm). Note that the small δ relative to g_{avg}, in combination with the magnitude of ℓ_{Fe}^{G}, accounts for the overall low C_{Fe} even in heavily annealed samples (at the 10–100 ppm level).

On the left axis of Fig. 4(e), the T_A dependence of ℓ_{Fe} is then compared with $\alpha_{eff}(T = 5\,\mathrm{K})/\alpha_{max}$. The dashed line is a guide to the eye, while the red circle is $\alpha_{eff}(T = 5\,\mathrm{K})$ for the Al IL device, for which the Kondo suppression is negligible. These compiled data (which include numerous T_A values in addition to the 80, 450, and 500 °C discussed thus far), reveal that only weak interdiffusion occurs below $T_A \approx 300\,°C$ (dotted line), with a commensurately modest impact on α_{eff}. An annealing effect is nevertheless noticeable, and clearly impacts ΔR_{NL} (see Ref. [20] and Figs. 1(a), 1(d), and 2(a)). Above about 300 °C, however, interdiffusion turns on rapidly, resulting in tens of parts per million $\langle C_{Fe}\rangle$ values, strong Kondo effects in both charge and spin transport, and a large decrease in the low T value of α_{eff}. This onset of strong interdiffusion will undoubtedly modify $\alpha_{eff}(T)$, even in the absence of Kondo effects. However, we note that while the modified spin polarization may have a T dependence that is not bulklike (e.g., resembling an Fe-Cu alloy over pure Fe), only the Kondo effect will lead to the nonmonotonic behavior that we observe. For such an alloy α will monotonically decrease with increasing T, likely with a stronger T dependence than pure Fe, and so the suppression due to the Kondo effect may, in fact, be *larger* than it appears in Fig. 1(d).

In general, relating the Kondo suppression of spin polarization (which is not yet on a firm theoretical footing) with a concentration profile across an FM/NM interface, and into the NM, is a nontrivial exercise. A plot of the type shown

in Fig. 4(e), however, reduces the problem to comparing only two independent parameters: the suppression in effective injection efficiency and the interdiffusion length. Quantifying the $\ell_{Fe} - \alpha_{eff}$ relation in this manner thus provides a compact summary of the influence of the FM/NM interface chemical profile on the Kondo-suppressed spin polarization in NLSVs, posing a well-defined challenge to future theoretical treatments of spin relaxation via the Kondo effect. More broadly, this method of correlating both spin and charge transport with chemical and structural characterization provides a precise means to isolate and determine the mechanisms limiting spin diffusion in metals and may thus be useful in future work.

APPENDIX: EXTRACTING α_{eff} FROM $\Delta R_{NL}(d)$

In the main text, only normalized values of α_{eff} are discussed, as in Fig. 1(d). For completeness, the extracted absolute values are shown in Fig. 5. While we believe these data provide a useful reference, we emphasize the caution that must be taken in interpreting them. In particular, although λ_N may be extracted uniquely using the d dependence of
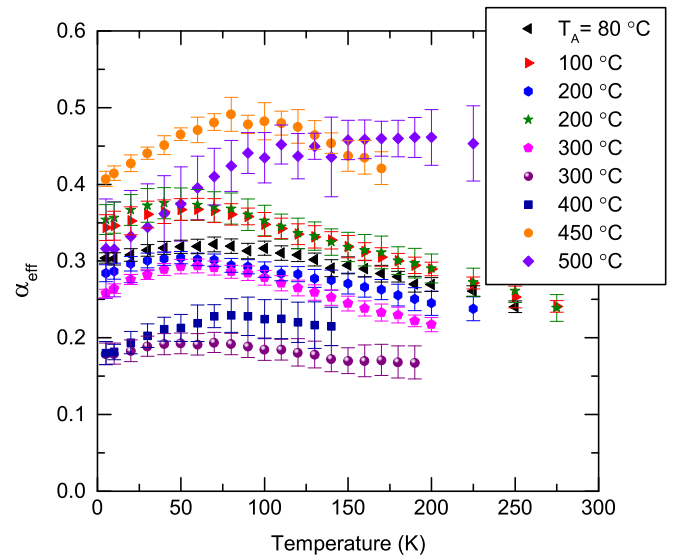

FIG. 5. Extracted $\alpha_{eff}(T)$ from fitting $\Delta R_{NL}(d,T)$ using Eq. (1), with $\lambda_{FM} = 4$ nm, for various T_A. Error bars indicate uncertainty in fitting, combined with error due to variation in measured FM and NM dimensions. Despite variation in the absolute magnitude, the Kondo contribution (as measured by the relative suppression at low T) monotonically increases with T_A.

$\Delta R_{\rm NL}$, the *magnitude* of α can easily suffer from a number of systematic errors and so should be viewed in light of such limitations. Specifically, although $\rho_{\rm FM}$ and ρ_N are measured directly or on nominally identical nanowires, variation in interface resistance R_I, $\lambda_{\rm FM}$, or $\alpha_{\rm FM}$ on annealing will all alter the magnitude of the observed $\Delta R_{\rm NL}$ at all separations and so will be manifest in the absolute value of the extracted

values of $\alpha_{\rm eff}$ for our fitting method. The variations in $\alpha_{\rm eff}$ we observe with T_A could, in fact, easily be accounted for with interface resistance, R_I, changes $\leqslant 2$ $R_{\rm FM}$. These would be largely undetectable by any transport measurement and would still maintain the condition of transparency, $R_I \sim R_{\rm FM} < R_N$. We note that all analysis here was done with a single fixed $\lambda_{\rm FM}$ value of 4 nm.

[1] M. Julliere, Phys. Lett. A **54**, 225 (1975).

[2] J. S. Moodera, L. R. Kinder, T. M. Wong, and R. Meservey, Phys. Rev. Lett. **74**, 3273 (1995).

[3] S. Yuasa, T. Nagahama, A. Fukushima, Y. Suzuki, and K. Ando, Nat. Mater. **3**, 868 (2004).

[4] S. S. P. Parkin, C. Kaiser, A. Panchula, P. M. Rice, B. Hughes, M. Samant, and S.-H. Yang, Nat. Mater. **3**, 862 (2004).

[5] J. Bass and W. P. Pratt, J. Phys. Condens. Matter **19**, 183201 (2007).

[6] M. Johnson and R. H. Silsbee, Phys. Rev. Lett. **55**, 1790 (1985).

[7] F. J. Jedema, A. T. Filip, and B. J. van Wees, Nature **410**, 345 (2001).

[8] R. J. Elliott, Phys. Rev. **96**, 266 (1954).

[9] F. Beuneu and P. Monod, Phys. Rev. B **18**, 2422 (1978).

[10] P. Monod and F. Beuneu, Phys. Rev. B **19**, 911 (1979).

[11] T. Kimura, T. Sato, and Y. Otani, Phys. Rev. Lett. **100**, 066602 (2008).

[12] E. Villamor, M. Isasa, L. E. Hueso, and F. Casanova, Phys. Rev. B **87**, 094417 (2013).

[13] H. Zou and Y. Ji, Appl. Phys. Lett. **101**, 082401 (2012).

[14] Y. Otani and T. Kimura, Philos. Trans. A. Math. Phys. Eng. Sci. **369**, 3136 (2011).

[15] M. Erekhinsky, F. Casanova, I. K. Schuller, and A. Sharoni, Appl. Phys. Lett. **100**, 212401 (2012).

[16] F. Casanova, A. Sharoni, M. Erekhinsky, and I. K. Schuller, Phys. Rev. B **79**, 184415 (2009).

[17] T. Kimura, N. Hashimoto, S. Yamada, M. Miyao, and K. Hamaya, NPG Asia Mater. **4**, e9 (2012).

[18] J. Kondo, Prog. Theor. Phys. **32**, 37 (1964).

[19] J. Kondo, *The Physics of Dilute Magnetic Alloys* (Cambridge University Press, Cambridge, 2012).

[20] L. O'Brien, M. J. Erickson, D. Spivak, H. Ambaye, R. J. Goyette, V. Lauter, P. A. Crowell, and C. Leighton, Nat. Commun. **5**, 3927 (2014).

[21] J. T. Batley, M. C. Rosamond, M. Ali, E. H. Linfield, G. Burnell, and B. J. Hickey, Phys. Rev. B **92**, 220420(R) (2015).

[22] S. Takahashi and S. Maekawa, Phys. Rev. B **67**, 052409 (2003).

[23] T. Valet and A. Fert, Phys. Rev. B **48**, 7099 (1993).

[24] F. J. Jedema, M. V. Costache, H. B. Heersche, J. J. A. Baselmans, and B. J. van Wees, Appl. Phys. Lett. **81**, 5162 (2002).

[25] Y. Ji, A. Hoffmann, J. S. Jiang, J. E. Pearson, and S. D. Bader, J. Phys. D. Appl. Phys. **40**, 1280 (2007).

[26] J. A. Mydosh, *Spin Glasses: An Experimental Introduction* (Taylor & Francis, London, 1993).

[27] M. Daybell and W. Steyert, Phys. Rev. **167**, 536 (1968).

[28] M. Erekhinsky, A. Sharoni, F. Casanova, and I. K. Schuller, Appl. Phys. Lett. **96**, 022513 (2010).

[29] For these devices, $T_{\rm min} \sim T_K \ll T_D$ (the Debye temperature). As $\rho_N(T)$ is fit near the Kondo minimum, contributions from both the full phenomenological expression (Ref. [38]) of the Kondo effect and Debye model of phonon scattering may be approximated by Eq. (2).

[30] This is obtained by simply using $\frac{\partial \rho_N}{\partial T}|_{T=T_{\rm min}} = 0 = 5AT_{\rm min}^{4} - \frac{\rho_K T_K}{T_{\rm min}}$, which then yields $T_{\rm min} = (\frac{T_K \rho_K}{5A})^{1/5}$.

[31] J. P. Franck, F. D. Manchester, and D. L. Martin, Proc. R. Soc. A **263**, 494 (1961).

[32] J. C. Fisher, J. Appl. Phys. **22**, 74 (1951).

[33] Y. Mishin and C. Herzig, Mater. Sci. Eng. A **260**, 55 (1999).

[34] G. Salje and M. Feller-Kniepmeier, J. Appl. Phys. **49**, 229 (1978).

[35] J. Mullen, Phys. Rev. **121**, 1649 (1961).

[36] C. Mackliet, Phys. Rev. **109**, 1964 (1958).

[37] T. Hutchison and J. Reekie, Phys. Rev. **83**, 854 (1951).

[38] D. Goldhaber-Gordon, J. Göres, M. A. Kastner, H. Shtrikman, D. Mahalu, and U. Meirav, Phys. Rev. Lett. **81**, 5225 (1998).